Journal of Alloys and Compounds 787 (2019) 759–766

Contents lists available at ScienceDirect

Journal of Alloys and Compounds

journal homepage: http://www.elsevier.com/locate/jalcom

Enhance supercapacitive performance of MnO_2/3D carbon nanotubes-graphene as a binder-free electrode

Tiantian Bi [a, b], Huaqing Fang [b], Jinlong Jiang [a, b, *], XingXing He [b], Xuan Zhen [b], Hua Yang [b], Zhiqiang Wei [b], Zhengfeng Jia [c]

[a] State Key Laboratory of Advanced Processing and Recycling of Nonferrous Metals, Lanzhou University of Technology, Lanzhou, 730050, China
[b] Department of Physics, School of Science, Lanzhou University of Technology, Lanzhou, 730050, China
[c] College of Materials Science and Engineering, Liaocheng University, Liaocheng, 252059, China

ARTICLE INFO

Article history:
Received 20 December 2018
Received in revised form
3 February 2019
Accepted 10 February 2019
Available online 11 February 2019

Keywords:
3D carbon nanotubes-graphene
Manganese oxide
Thermal decomposition
Supercapacitor

ABSTRACT

In this paper, the MnO_2/three-dimensional carbon nanotubes-graphene nanocomposite was synthesized on Cu foil substrate by chemical vapor deposition and subsequent thermal decomposition of manganese acetyllacetonate precursors. The nanocomposite material was directly used as a binder-free electrode to investigate the supercapacitive performance. The results indicate that the appropriate defects and MnO_2 nanoparticles are introduced simultaneously into the carbon nanotubes-graphene architecture in one-step. The specific capacitance of MnO_2/three-dimensional carbon nanotubes-graphene/Cu electrode is up to 365 F g^{-1} at a current density of 1 A g^{-1} in 1.0 M Na_2SO_4 solution, which is 9 times higher than that of electrode without MnO_2 modification. After 1000 cycles at 1 A g^{-1}, the capacity retention is still maintained at 97.0%, suggesting potential applications in high-performance energy storage devices. The excellent electrochemical performances of nanocomposite electrode can be attributed to the significantly synergistic effects between the lasting electronic conductivity of three-dimensional carbon nanotubes-graphene/Cu with the appropriate defects and the pseudocapacitance of the MnO_2 nanoparticles.

1. Introduction

Energy storage materials and technology have become one of the most important topics with the utilization of mobile electronic devices and the development of renewable energy sources in recent years [1–3]. As the most important electrochemical energy storage devices, supercapacitors have been widely investigated because of their low cost, high power density, long cycle life, and fast dynamic responses. Carbon-based nanomaterials such as carbon nanotubes (CNTs) and graphene have been extensively used as the effective electrodes of electrochemical double-layer capacitors (EDLCs), owing to high specific surface area, excellent electrical conductivity, high mechanical strength, and good electrochemical stability in a large variety of electrolytes [4–6]. Especially, the flexible lightweight carbon-based supercapacitors would satisfy the implantable and wearable electronics in the future [7–9]. Recent studies have indicated that three-dimensional CNTs-graphene (3D CNTs-G) architecture with a covalently bonded junction is a promising candidate for application in energy storage, electronic devices and environment due to desirable out-of-plane transport and mechanical properties [10–15]. However, the most of the reported hybrid structures demonstrated the low surface area utilization efficiency due to morphologies of bundles [16], fibers [17] and carpets [18,19] assembled by single nanotubes under van der Waals interactions, which could make it difficult to perform better on electrochemical energy storage. Recently, some works have been made to address this problem. Zhang et al. [20] reported that the vertically aligned multi-walled CNT carpets were split and expanded by potassium vapor. The split CNT carpets exhibited the enhanced electrochemical performance with better specific capacitance in a supercapacitor owing to the increased surface areas for ion accessibility. Shi et al. [21] introduced the defects on the surface of CNT forest by annealing in air. The defective CNT forest demonstrated a hydrophilic surface that is easier to contact with the electrolyte, and thus improving the electrochemical performance.

Incorporating transition-metal oxides such as MnO_2 [22–25],

* Corresponding author. State Key Laboratory of Advanced Processing and Recycling of Nonferrous Metals, Lanzhou University of Technology, Lanzhou, 730050, China.
E-mail address: golden_dragon@126.com (J. Jiang).

https://doi.org/10.1016/j.jallcom.2019.02.117
0925-8388/

Co_3O_4 [26], NiO [27], and $NiCo_2O_4$ [28] into 3D CNTs-G hybrid material has been considered to be another effective way to improve the specific capacitance of carbon-based electrodes, because of their large theoretical faradic pseudocapacitance. Among these available pseudocapacitive materials, MnO_2 is particularly attractive for application due to its natural abundance, low cost, high capacitance and environmental compatibility. The incorporation of α, β, γ and δ structured MnO_2 on CNTs can be realized through chemical co-precipitation, electrophoretic, electrochemical deposition and thermal decomposition [29–33]. Thermal decomposition is a facile route to prepare MnO_2-CNTs composite electrodes. Fan et al. [34] reported that MnO_2 was synthesized and dispersed on CNT matrix by thermal decomposing $Mn(NO_3)_2$. Recently, Cui et al. [35] prepared the uniformly dispersed Mn_3O_4 nanoparticles within CNT array by thermal decomposition of $Mn(CH_3COO)_2{\cdot}4H_2O$. The maximum specific capacitance of the composite electrode reached to 143 F g^{-1} at scan rate of 2 mV s^{-1}. The specific capacitance retained 77–81% of the original value after 1000 cycles at a scan rate of 50 mV s^{-1}.

In light of the above considerations, the electrochemical performance of 3D CNTs-G hybrid materials could be enhanced from morphologies and structures (dispersion, defects) of CNTs-G, and modification of metal oxides. However, most of the reports involved the two steps including surface oxides in acid solution or in air at elevated temperatures, and the subsequent composite process. So far, no method has been reported to simultaneously introduce the numerous defects and MnO_2 nanoparticles in 3D CNTs-G hybrid material by thermal decomposing manganese acetyllacetonate in one-step.

The 3D hybrid materials were usually fabricated on foam nickel, titanium, and carbon cloth substrates as binder-free electrodes [36–38]. Although copper has a better electrical conductivity, few studies have been reported copper foil as electrodes since it is easily to react with electrolyte. In this study, the 3D CNTs-G with covalently bonded interface grown directly on Cu foil as binder-free integrated electrode (3D CNTs-G/Cu) for supercapacitors, which can provide more efficient electron transport at interface than traditional slurry-derived electrodes. The α-MnO_2 nanoparticles have been synthesized to modify the 3D CNTs-G architecture (MnO_2/3D CNTs-G/Cu) through a facile thermal decomposing $Mn(acac)_3{\cdot}4H_2O$ method. Simultaneously, the 3D CNTs-G architecture exhibits the increased defects in structure and more dispersed bundles in morphologies, which provides larger surface area and rich active sits for electrochemical reactions as well as the effective transport of electrolyte ions in electrode materials.

2. Experimental section

2.1. Preparation of MnO_2/3D CNTs-G/Cu electrode

The synthesis schemes of MnO_2/3D CNTs-G/Cu electrode are illustrated in Fig. 1. The 3D CNTs-G hybrid material was constructed on Cu foil substrate through the successive growing multi-layer graphene and multi-wall CNTs using chemical vapor deposition (CVD) method. The multi-layer graphene was grown on Cu foil for 15 min at 1000 C° under mixture atmosphere of 10 sccm CH_4 and 300 sccm H_2. The multi-wall CNTs were grown for 15 min under an atmosphere of 2 sccm C_2H_2 and 210 sccm H_2 using the catalysts of Fe and the buffer layer of Al_2O_3. The synthesis process was described in details previously [13]. The as-prepared 3D CNTs-G/Cu hybrid material was employed as substrate for synthesizing MnO_2 nanoparticles via a thermal decomposition process. Typically, 70 mg of $Mn(acac)_3{\cdot}4H_2O$ were dissolved in 10 mL of ethylene glycol by ultra-sonication 30 min. The 3D CNTs-G/Cu sample was immersed into the $Mn(acac)_3{\cdot}4H_2O$–$C_6H_{14}O_2$ solution for 24 h. Subsequently, the sample was taken out and dried in a vacuum oven at 50 °C for 24 h. Finally, the 3D-CNT-G/Cu loaded with $Mn(acac)_3{\cdot}4H_2O$ was heated in a tube furnace from room temperature to 410 °C at a heating rate of 10 °C under air atmosphere. The sample was quickly removed from the hot region and permitted to cool to room temperature.

2.2. Materials characterization

The surface morphology of the samples was observed using a field-emission scanning electron microscope (FESEM, JSM-6701F) equipped with an Oxford INCA X-ray energy dispersive spectrometer (EDS) at an accelerating voltage of 5 kV. The crystallographic structure were characterized by powder X-ray diffraction (XRD, Bruker D8 ADVANCE) instrument. The high-resolution transmission electron microscopy (HRTEM) images were acquired using an electron microscopy (FEI Tecnai G2F20). Raman spectra were recorded using a confocal Raman spectrometer (LabRAM HR Evolution) with a wavelength of 532 nm. X-ray photoelectron spectra (XPS) were collected using spectrometer (Escalab 250Xi) with monochromated Al $K\alpha$ radiation. Thermo gravimetric analysis (TGA) and differential thermal analysis (DTA) were performed from room temperature to 700 °C in air at a heating rate of 10 °C min^{-1} using a thermoanalyser (NetzschSTA-409C). The Brunauer-Emmett-Teller (BET) surface area and Barret-Joyner-Halenda (BJH) pore size distribution curve of MnO_2/3D CNTs-G were measured at −197 °C by an apparatus (Micromeritics ASAP 2020).

2.3. Electrochemical measurements

The electrochemical properties of the samples were carried out in a three-electrode cell system using a CS350H electrochemical workstation (Wuhan Corrtest Instrument, China) at room temperature [39,40]. The MnO_2/3D CNTs-G/Cu sample with an area of 0.2 cm^2 was used directly as a binder-free working electrode. The mass of the 3D CNTs-G and MnO_2/3D CNTs-G materials were calculated to be 0.08 mg and 0.1 mg, respectively. A saturated calomel electrode (SCE) and a platinum foil were used as the reference electrode and the counter electrode in a 1.0 M Na_2SO_4 aqueous solution, respectively.

Cyclic voltammogram (CV) and galvanostatic charge-discharge (GCD) curves were acquired in the potential range from −0.6 to 0 V at different scanning rates and current densities. The electrochemical impedance spectroscopy (EIS) measurement was conducted in the amplitude of 10 mV at the open circuit potential. The specific capacitance was calculated from the charge-discharge curves using the following equation:

$$C_s = \frac{I\Delta t}{m\Delta V}$$

where I is the discharging current (A), Δt is the discharge time (s), ΔV is the potential window (V), and m is the mass of active material in the working electrode (g).

3. Results and discussion

Fig. 2a shows the curves of TG and DTA of $Mn(acac)_3{\cdot}4H_2O$ under air atmosphere. The weight loss of ~20% below 160 °C is attributed to evaporation of residual ethylene glycol, adsorbed and hydrated water molecules [41,42]. The decomposition of $Mn(acac)_3$ occurred above 160 °C due to the fractional decomposition of acetylacetonate group. The weight loss of ~30% is observed in range of ~320–410 °C, which may be due to the complete decomposition of $Mn(acac)_3$ leading to the formation of MnO_2 phase [43]. Therefore,

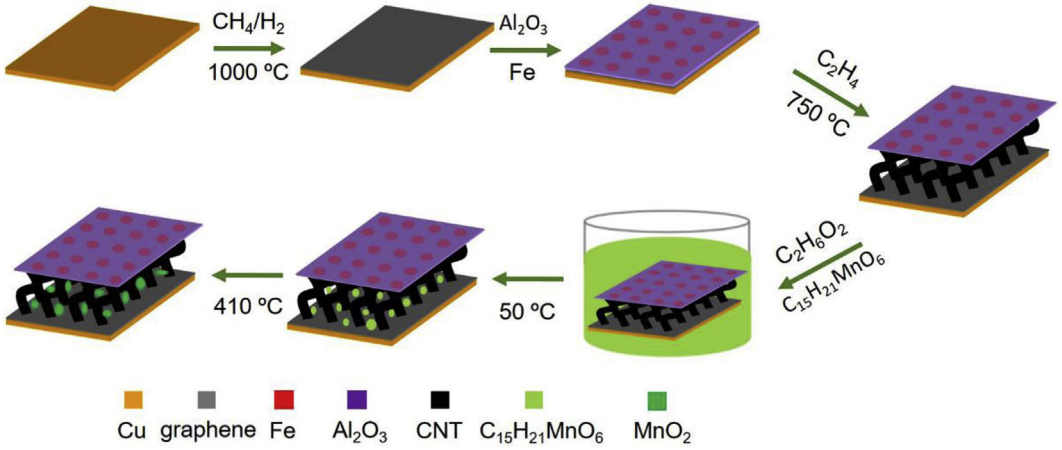

Fig. 1. Schematic illustration for preparation of the binder-free MnO2/3D CNTs-G/Cu electrode.

in this study the decomposition was conducted at 410 °C for the fabrication of MnO_2/3D CNTs-G/Cu electrode. Fig. 2b shows the BET surface area and BJH pore size distribution curve of MnO_2/3D CNTs-G. The specific surface area of the sample is as high as 119.6 $m^2 g^{-1}$, which should facilitate the formation of double layers at the electrode/electrolyte interface. The sample has a hierarchical meso-macro pore size distribution with the average pore size of 40 nm in the range of 2–100 nm. Since micropores are not easily accessible by electrolyte ions, while macropores are simply too large leading to a reduced specific surface area [44], the MnO_2/3D CNTs-G dominated by the mesopores centered at 15 nm can provide effective paths for electrolyte ion transport.

Fig. 3a–d shows the top-view SEM images of 3D CNTs-G/Cu and MnO_2/3D CNTs-G/Cu samples. The CNTs exist as tightly packed bundles for 3D CNTs-G/Cu sample. The residual Fe/Al_2O_3 catalyst can be found on the tip of the curved CNTs bundles, suggesting a tip-growth mechanism. After introducing MnO_2, the bundles of CNTs become thicker and coarse due to the increase of dispersion for MnO_2/3D CNTs-G/Cu sample, which may be beneficial for faster transport of electrolyte ions during the electrochemical process. Fig. 3e–g shows the elemental mapping images and EDS spectra of MnO_2/3D CNTs-G/Cu sample. The elemental distribution of Mn and O implies that the MnO_2 derived from decomposition is quite uniform in 3D CNTs-G.

Fig. 4a shows the XRD pattern of MnO_2/3D CNTs-G/Cu electrode. The diffraction peaks at 43.4° and 50.5° correspond to the (111) and (200) planes of face-centered cubic Cu. The weak peaks at 36.6°, 42.5°, 61.7° and 73.4° were assigned to (111), (200), (220) and (311) planes of cubic Cu_2O (JCPDS No. 05–667), which implies that the exposed surface of the Cu foil was oxidized partially at high temperature. The unexposed surface of Cu foil was protected by graphene and CNTs, forming a good electric contact at interface. Thus, the Cu foil with passivation surface can be used as a sable collector in Na_2SO_4 solution. No diffraction peak of MnO_2 is observed which could be due to the low content in the sample. Fig. 4b shows the Raman spectra of G/Cu, CNTs-G/Cu and MnO_2/3D CNTs-G/Cu. The peaks observed in the range of 1000–1800 cm^{-1} are typical D and G peaks of carbon materials [45,46]. The G peak originates from first-order scattering of the E_{2g} phonons of sp^2-hybridized carbon atoms, while the D peak is due to the breathing mode of k-point photons of A_{1g} symmetry that related to the defects [47]. The strong G peak at 1585 cm^{-1} accompanied by the weak D peak at 1350 cm^{-1} indicates that the high-quality graphene was grown on Cu substrate. After CNTs growth, the D and G peaks shift slightly to 1330 cm^{-1} and 1578 cm^{-1} in CNTs-G/Cu sample. Significantly, G peak shifts to higher wavenumbers, meanwhile the intensity ratio of D peak to G peak (I_D/I_G) increases from 0.24 for 3D CNTs-G/Cu to 0.57 for MnO_2/3D CNTs-G/Cu. This suggests increase of the defects owing to the calcination in air, as the oxygen and $Mn(acac)_3$ molecules could etch CNTs and graphene at high temperature [33]. Obviously, the high defect density would be favorable for the enhancement of electrochemical performance as long as 3D CNTs-G can provide the lasting electrical conducting and mechanical supporting for MnO_2 [21,48]. Moreover, the weak peak centered at 640 cm^{-1} in the low wavenumbers is correlated to the Mn–O symmetric stretching vibration [49], further implying the presence of MnO_2 in 3D CNTs-G/Cu.

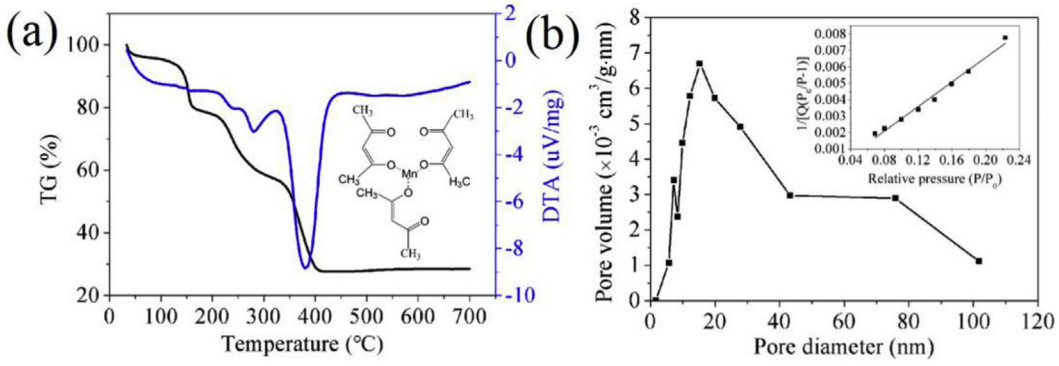

Fig. 2. (a) TG-DTA curves of $Mn(acac)3 \cdot 4H_2O$ under air atmosphere, (b) BET surface area and BJH pore size distribution of MnO_2/3D CNTs-G.

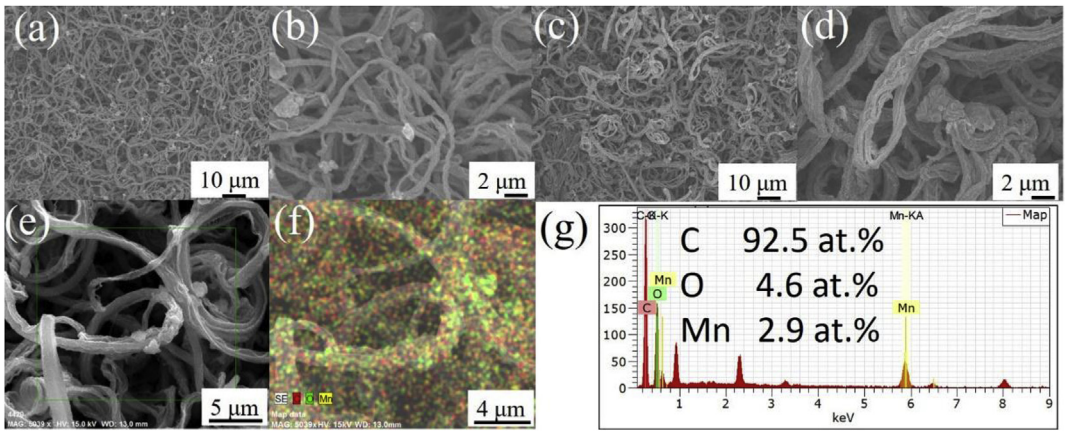

Fig. 3. (a, b) SEM images of 3D CNTs-G/Cu; (c, d) SEM images, (e, f) elemental mapping images and (g) EDS spectra of MnO_2/3D CNTs-G/Cu sample.

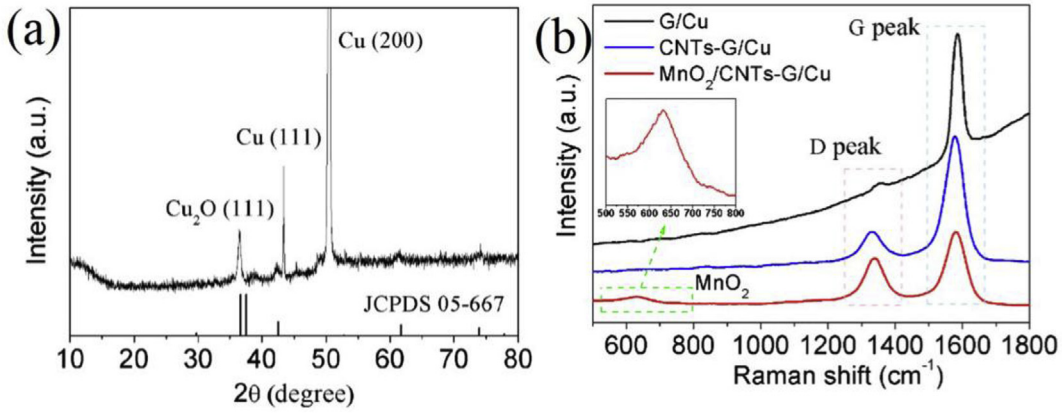

Fig. 4. (a) XRD pattern of MnO_2/3D CNTs-G/Cu and (b) Raman spectra of G/Cu, CNTs-G/Cu and MnO_2/3D CNTs-G/Cu.

XPS spectra obtained from MnO_2/3D CNTs-G/Cu and 3D CNTs-G/Cu are shown in Fig. 5. The Mn $2p_{3/2}$ peak centered at 642.3 eV and Mn $2p_{1/2}$ peak at 654.0 eV with a spin-energy separation of 11.7 eV are in good agreement with the binding energy of MnO_2 [50]. The Mn—O bonding in MnO_2 can be clearly observed at 530.3 eV from the O 1s spectrum in Fig. 5b. In order to compare the variation of 3D CNTs-G and MnO_2/3D CNTs-G/Cu, the C 1s spectra was deconvoluted into three components at 284.8, 285.9 and 288.4 eV, corresponding to C—C C—O, C═O bonds, respectively [51,52]. The full width at half maximum (FWHM) of C—C peak increased remarkably from 0.8 for 3D CNTs-G/Cu to 1.2 for MnO_2/3D CNTs-G/Cu, which implies that the defects such as sp^3-hybridized carbon atoms were introduced into 3D CNTs-G matrix.

Fig. 6 show the HRTEM images and the selected-area electron diffraction (SAED) pattern of MnO_2/3D CNTs-G. The CNTs in close contact with a graphene sheet can be observed in Fig. 6a. The nanosized MnO_2 nanoparticles were anchored or encapsulated between adjacent CNTs, as shown in Fig. 6b. The selected-area electron diffraction (SAED) pattern (Fig. 6c) shows that the MnO_2 derived from thermal decomposition is polycrystalline nature with a tetragonal crystal structure. In Fig. 6d, the lattice fringes with the spacing of 0.34 nm and 0.18 nm are in agreement with the (002) plane of CNTs and the (411) plane of α-MnO_2, respectively. Fig. 6e and f shows the HRTEM images of a CNT with defects. The amorphous structure and the peeled graphene layer can be clearly seen on the nanotube walls, which provides a direct proof of introducing defects in 3D CNTs-G via a facile thermal decomposing process.

Fig. 7a shows the cyclic voltammetry (CV) curves of 3D CNTs-G/Cu at scan rates of 10, 20, 50, 100, and 200 mV s^{-1} with a voltage window of -0.6—0 V. The CV curves exhibit rectangular-like shape with a few humps, which is a typical double-layer capacitive behavior of carbon-based electrode. This is confirmed by the nearly triangular charge-discharge curve at current density of 1, 5, 10 and 20 A g^{-1} in Fig. 7c. As shown in Fig. 7b, the MnO_2/3D CNTs-G/Cu electrode exhibits much larger rectangle area of CV curves at the same scan rate compared to the 3D CNTs-G/Cu electrode, which indicates a superior capacitive performance. The rectangular-like curves are maintained even at an ultrahigh scan rate of 200 mV s^{-1}, suggesting that the pseudocapacitive reaction is fast and reversible. The charge-discharge curves with nearly linear but a large distortion indicates the pseudocapacitance contribution of the MnO_2/3D CNTs-G/Cu electrode due to redox process. The specific capacitances of both 3D CNTs-G/Cu and MnO_2/3D CNTs-G/Cu electrodes were calculated at various current density from the galvanostatic charge-discharge (GCD) curves, and the results are shown in Fig. 7e. The specific capacitance of 3D CNTs-G/Cu electrode is 42.3 F g^{-1} at current density of 1 A g^{-1}, which is close to data in literature [20,53]. The specific capacitance of pure MnO_2 derived by thermal decomposition is 30 F g^{-1} at current density of 1A g^{-1}. The specific capacitance of MnO_2/3D CNTs-G/Cu electrode increases remarkably to 365 F g^{-1}, which is about nine times that of 3D CNTs-G/Cu and twelve times that of pure MnO_2. This specific capacitance is also higher than that of other MnO_2/CNTs composite electrodes reported in literature [54,55]. As the current density

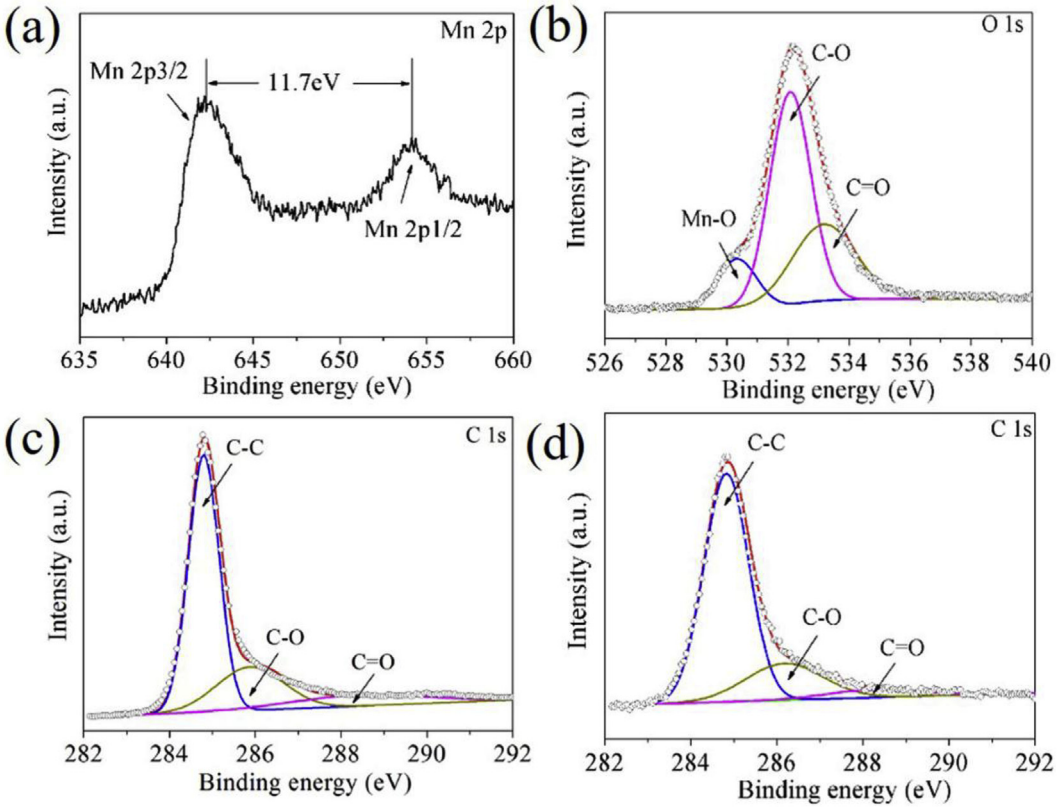

Fig. 5. XPS spectra of (a) Mn 2p, (b) O 1s and (c) C 1s of MnO2/3D CNTs-G/Cu, and (d) C 1s of 3D CNTs-G/Cu.

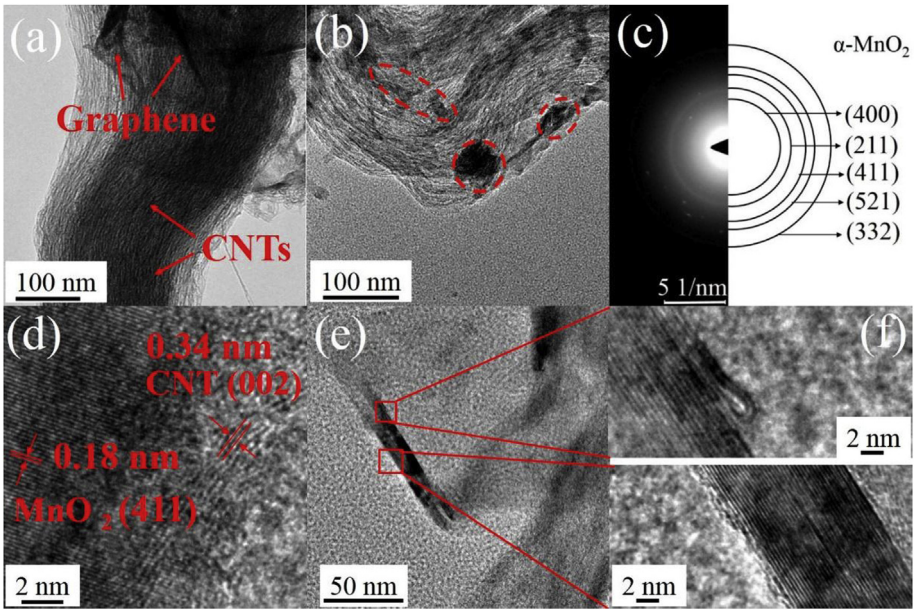

Fig. 6. (a, b) TEM images, (c) SAED pattern and (d–f) HRTEM images of MnO2/3D CNTs-G.

increases to 20 A g^{-1}, the composite electrode still maintains a reversible capacitance as high as 287 F g^{-1}, implying the excellent rate capability. EIS was used to analyze the kinetics of the interaction between electrode and electrolyte for supercapacitors. Fig. 7f shows the Nyquist plots of 3D CNTs-G/Cu and MnO_2/3D CNTs-G/Cu electrodes. The equivalent circuit of the working electrode are shown in the illustration. R_s represents the equivalent series resistance depending on the electrolyte resistance, electrode resistance and the contact resistance at the interface between electrodes and the current collector [56]. The R_s value of MnO_2/3D CNTs-G/Cu electrode is close to that of 3D CNTs-G/Cu electrode, indicating that the thermal decomposing did not lead to the degeneration on electrical conductivity of 3D CNTs-G/Cu electrode.

The semicircle diameter in the high-frequency region

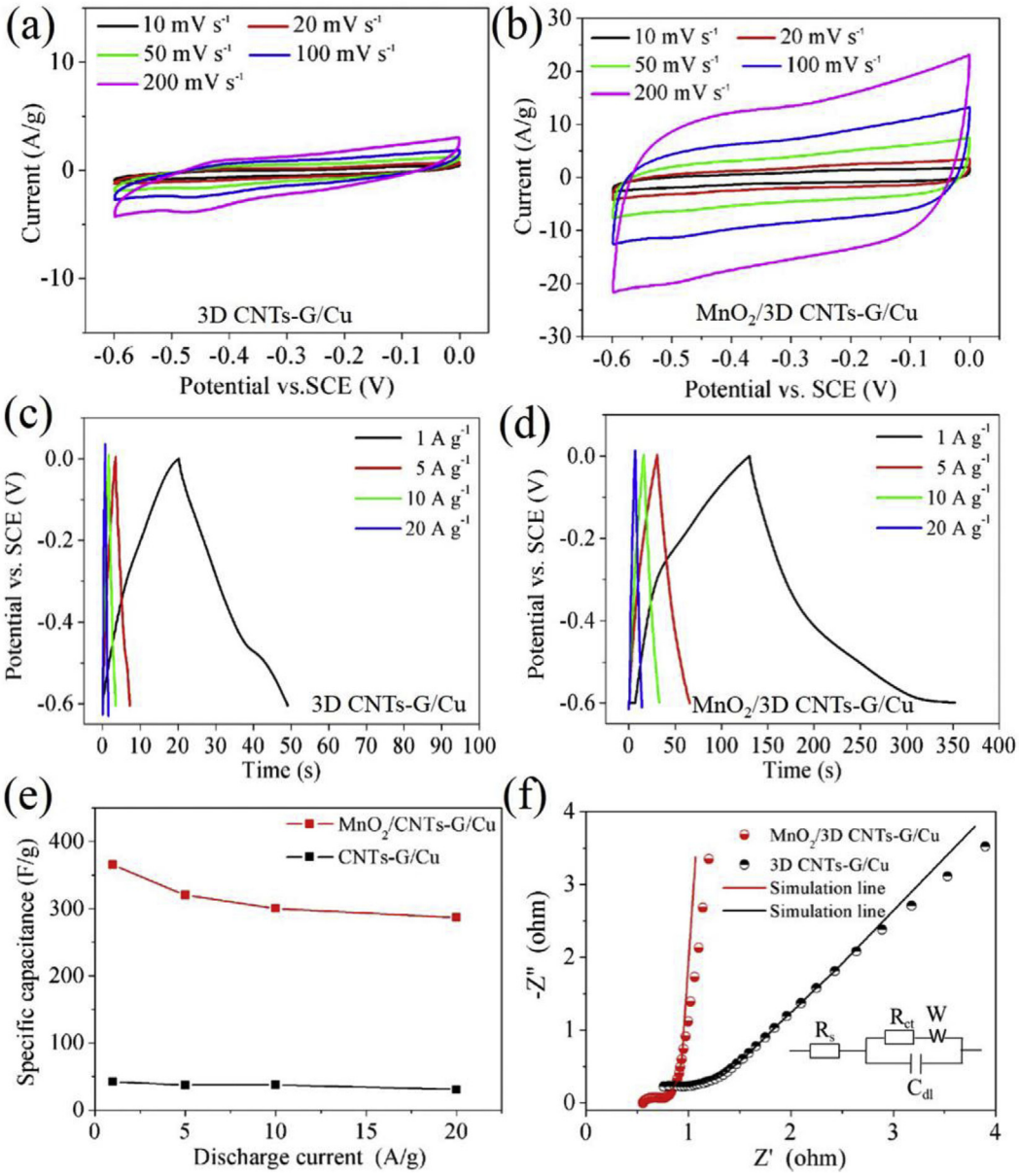

Fig. 7. (a, b) CV curves at different scan rates, (c, d) galvanostatic charge-discharge curves and (e) gravimetric capacitance at different current density, and (f) Nyquist plots in 1.0 M Na2SO4 of 3D CNTs-G/Cu and MnO2/3D CNTs-G/Cu electrodes.

corresponds to the charge-transfer resistance (R_{ct}) caused by the Faradaic reaction at the surface and interfaces. The R_{ct} value of MnO_2/3D CNTs-G/Cu electrode (0.23 Ω) is much lower than those of the MnO_2/CNTs (0.6–2 Ω) electrodes synthesized by liquid-phase methods [57–59], suggesting that the MnO_2/3D CNTs-G/Cu electrode has an easier electrolyte ion access and electron transport behavior. C_{dl} corresponds to the capacitance of the electrode, and W is the Warburg impedance which reflected the ion diffusion in the electrode.

The long-term cycling stability of the MnO_2/3D CNTs-G/Cu electrode was further performed at a current density of 1.0 A g^{-1}, as shown in Fig. 8a. The special capacitance undergoes a slight fluctuation and reaches a stable value after initial charge-discharge 100 cycles. After 1000 cycles, the MnO_2/3D CNTs-G/Cu electrode exhibits an excellent long-term cycling stability with 97.0% capacitance retention, indicating that the repetitive charge-discharge cycles do not induce noticeable degradation of the microstructure. Furthermore, the coulombic efficiency is over 97.6% during the cycling process, implying the excellent charge-discharge reversibility and high energy efficiency. The Nyquist plots of the electrode before and after cycles are very similar, but more vertical line in the low frequency region is observed in Fig. 8b after 1000 cycles due to the electrolyte fully penetrating into the electrode material.

The MnO_2/3D CNTs-G/Cu electrode exhibits superior capacitive performance with high specific capacitance and excellent cycling stability, which can be attributed to the synergistic effects of defective 3D CNTs-G with lasting conductivity and MnO_2 nanoparticles with high specific pseudocapacitance. Thus, the thermal decomposition conditions such as temperature and time need to be considered to exploit fully the inherent advantages of components in the MnO_2/3D CNTs-G/Cu. The MnO_2 nanoparticles could not provide a valid pseudocapacitance due to the incomplete decomposition of $Mn(acac)_3$ at low temperature. However, the 3D CNTs-G/

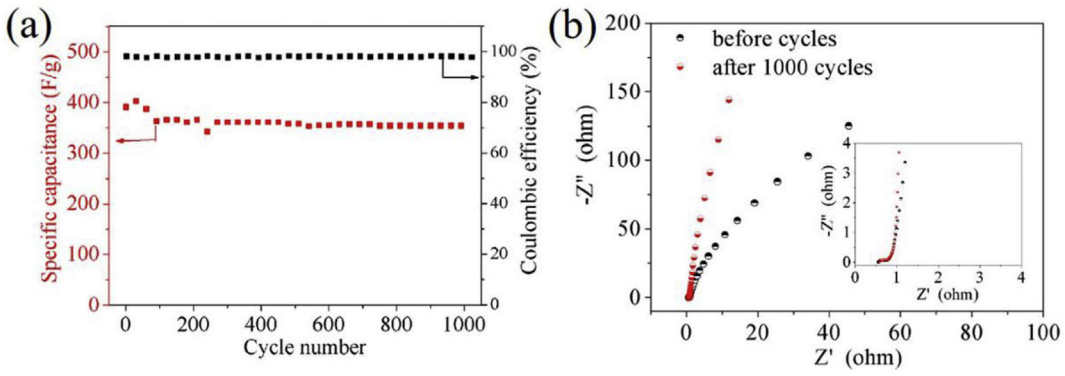

Fig. 8. (a) Capacitance retention and Coulombic efficiency after 1000 cycles at a current density of 1 A/g, (b) Nyquist plots of before and after 1000 cycles of MnO2/3D CNTs-G/Cu electrode.

Cu would not offer the reliable and effective conducting pathways for ions and electrons due to be oxidation and damage of CNTs and graphene at high temperature and long-time calcination. Actually, the active materials partially peeled off from Cu substrate, as the decomposing temperature for MnO_2/3D CNTs-G/Cu-10 sample is at 410 °C for 10 min. As shown in Fig. S1, the CV curves of MnO_2/3D CNTs-G/Cu-10 electrode exhibit a large distortion due to appearance of redox peak, suggesting that 3D CNTs-G structure was oxidized in air. In this case, the specific capacitance of 3D CNTs-G/Cu-10 electrode decreased to 141.7 $F g^{-1}$ at current density of 1 $A g^{-1}$, which can be attributed to the structure collapse of 3D CNTs-G.

4. Conclusions

In summary, a binder-free MnO_2/3D CNTs-G/Cu electrode has been successfully fabricated through the successive CVD process followed by a facile thermal decomposition method. The α-MnO_2 nanoparticles were formed in 3D CNTs-G by thermal decomposition of manganese acetyllacetonate precursors. Not only that, this process introduced appropriate defects and resulted in more dispersed bundles (larger surface area) in 3D CNTs-G structure, which can provide rich active sit for electrochemical reactions as well as the effective transport of electrolyte ions. Owing to the significantly synergistic effects between the lasting electronic conductivity of 3D CNTs-G/Cu with defects and the pseudo capacitance of the MnO_2 nanoparticles, the MnO_2/3D CNTs-G/Cu electrode exhibits a high specific capacitance of 365 $F g^{-1}$ at a current density of 1 $A g^{-1}$ and an excellent capacity retention of 97% after 1000 cycles. This work provides a facile synthetic strategy for the fabrication of the high-performance supercapacitor electrode materials by introducing the defects and transition metal oxide into carbon-based nanomaterials in one-step.

Notes

The authors declare no competing financial interest.

Acknowledgements

This work was supported by the National Natural Science Foundation of China (51741104). We also acknowledge support from the Hongliu first disciplines Development Program of Lanzhou University of Technology.

Appendix A. Supplementary data

Supplementary data to this article can be found online at https://doi.org/10.1016/j.jallcom.2019.02.117.

References

[1] Z. Lv, Y. Tang, Z. Zhu, J. Wei, W. Li, H. Xia, Y. Jiang, et al., Honeycomb lantern-inspired three-dimensional stretchable supercapacitors with enhanced specific areal capacitance, Adv. Mater. 30 (2018) 1805468.
[2] D. Selvakumar, A. Alsalme, A. Alswieleh, R. Jayavel, Freestanding flexible nitrogen doped-reduced graphene oxide film as an efficient electrode material for solid-state supercapacitors, J. Alloy. Compd. 723 (2017) 995–1000.
[3] S. Xin, N. Yang, F. Gao, J. Zhao, L. Li, C. Teng, Three-dimensional polypyrrole-derived carbon nanotube framework for dye adsorption and electrochemical supercapacitor, Appl. Surf. Sci. 414 (2017) 218–223.
[4] H. Pan, J. Li, Y.P. Feng, Carbon nanotubes for supercapacitor, Nanoscale Res. Lett. 5 (2010) 654–668.
[5] L. Wen, F. Li, H.-M. Cheng, Carbon nanotubes and graphene for flexible electrochemical energy storage: from materials to devices, Adv. Mater. 28 (2016) 4306–4337.
[6] W. Yang, M. Ni, X. Ren, Y.F. Tian, N. Li, Y.F. Su, et al., Graphene in supercapacitors applications, Curr. Opin. Colloid Interface Sci. 20 (2015) 416–428.
[7] Y. Jiang, Z. Liu, N. Matsuhisa, D. Qi, W.R. Leow, H. Yang, et al., Auxetic mechanical metamaterials to enhance sensitivity of stretchable strain sensors, Adv. Mater. 30 (2018) 1706589.
[8] C. Wan, G. Chen, Y. Fu, M. Wang, N. Matsuhisa, S. Pan, et al., An artificial sensory neuron with tactile perceptual learning, Adv. Mater. 30 (2018) 1801291.
[9] P. Cai, B. Hu, W.R. Leow, X. Wang, X.J. Loh, Y.-L. Wu, et al., Biomechano-interactive materials and interfaces, Adv. Mater. 30 (2018) 1800572.
[10] Y. Zhu, L. Li, C. Zhang, G. Casillas, Z. Sun, Z. Yan, et al., A seamless three-dimensional carbon nanotube graphene hybrid material, Nat. Commun. 3 (2012) 1225.
[11] Z. Yan, Lulu Ma, Y. Zhu, I. Lahiri, M.G. Hahm, Z. Liu, et al., Three-dimensional metal-graphene-nanotube-multifunctional hybrid materials, ACS Nano 7 (2013) 58–64.
[12] Y. Xue, Y. Ding, J. Niu, Z. Xia, A. Roy, H. Chen, et al., Rationally designed graphene-nanotube 3D architectures with a seamless nodal junction for efficient energy conversion and storage, Sci. Adv. 1 (2015) 1400198.
[13] J. Jiang, Y. Li, C. Gao, N.D. Kim, X. Fan, G. Wang, Z. Peng, et al., Growing carbon nanotubes from both sides of graphene, ACS Appl. Mater. Interfaces 8 (2016) 7356–7362.
[14] Y. Yang, N.D. Kim, Y. Varshney, S. Sihn, Y. Li, A.K. Roy, et al., In situ mechanical investigation of carbon nanotube-graphene junction in three-dimensional carbon nanostructures, Nanoscale 9 (2017) 2916.
[15] A. Dasgupta, L.P. Rajukumar, C. Rotella, Y. Lei, M. Terrones, Covalent three-dimensional networks of graphene and carbon nanotubes: synthesis and environmental applications, Nano Today 12 (2017) 116–135.
[16] Y.D. Lim, D. Grapov, L. Hu, Q. Kong, B.K. Tay, V. Labunov, et al., Enhanced field emission properties of carbon nanotube bundles confined in SiO_2 pits, Nanotechnology 29 (2018), 075205.
[17] H. Sun, X. You, J. Deng, X. Chen, Z. Yang, J. Ren, et al., Novel graphene/carbon nanotube composite fibers for efficient wire-shaped miniature energy devices, Adv. Mater. 26 (2014) 2868–2873.
[18] J. Ding, S. Fu, R. Zhang, E. Boon, W. Lee, F.T. Fisher, et al., Graphene-vertically aligned carbon nanotube hybrid on PDMS as stretchable electrodes, Nanotechnology 28 (2017) 465302.
[19] R.V. Salvatierra, D. Zakhidov, J. Sha, N.D. Kim, S.K. Lee, A.O. Raji, Splitting of a

vertical multi-walled carbon nanotube carpet to a graphene nanoribbon carpet and its use in supercapacitors, ACS Nano 11 (2017) 2724.
[20] C. Zhang, Z. Peng, J. Lin, Y. Zhu, G. Ruan, C.-C. Hwang, W. Lu, R.H. Hauge, J.M. Tour, ACS Nano 7 (2013) 5151.
[21] X. Shi, Y. Li, R. Chen, H. Ni, W. Zhan, B. Zhang, F. Zheng, S. Dong, Defective carbon nanotube forest grown on stainless steel encapsulated in MnO_2 nanosheets for supercapacitors, Electrochim. Acta 278 (2018) 61–71.
[22] C. Choi, H.J. Sim, G.M. Spinks, X. Lepró, R.H. Baughman, S.J. Kim, Elastomeric and dynamic MnO_2/CNT core-shell structure coiled yarn supercapacitor, Adv. Energy Mater. 6 (2016) 1502119.
[23] Y. Liu, X. Zhou, R. Liu, X. Li, Y. Bai, G. Yuan, Preparation of three-dimensional compressible MnO_2@carbon nanotubes sponges with enhanced supercapacitor performance, New J. Chem. 41 (2017) 14906–14913.
[24] X. Meng, L. Lu, C. Sun, Green synthesis of three-dimensional MnO_2/graphene hydrogel composites as a high performance electrode material for supercapacitors, ACS Appl. Mater. Interfaces 10 (2018) 16474–16481.
[25] P. Lv, X. Tang, W. Wei, Graphene/MnO_2 aerogel with both high compression-tolerance ability and high capacitance, for compressible all-solid-state supercapacitors, RSC Adv. 7 (2017) 47116–47124.
[26] Y.L. Yin, Y. Xu, Y. Zhou, Y. Yan, K. Zhan, J.H. Yang, et al., Millimeter-long vertically aligned carbon-nanotube-supported Co_3O_4 composite electrode for high-performance asymmetric supercapacitor, ChemElectroChem 5 (2018) 1394–1400.
[27] J.Y. Cheng, B. Zhao, W.K. Zhang, F. Shi, G.P. Zheng, D.Q. Zhang, et al., High-performance supercapacitor applications of NiO-nanoparticle-decorated millimeter-long vertically aligned carbon nanotube arrays via an effective supercritical CO_2-assisted method, Adv. Funct. Mater. 25 (2015) 7381–7391.
[28] H. Tong, S. Yue, L. Lu, F. Jin, Q. Han, X. Zhang, J. Liu, A binder-free $NiCo_2O_4$ nanosheet/3D elastic N-doped hollow carbon nanotube sponge electrode with high volumetric and gravimetric capacitances for asymmetric supercapacitors, Nanoscale 9 (2017) 16826–16835.
[29] W. Wei, X. Cui, W. Chen, D.G. Ivey, Manganese oxide-based materials as electrochemical supercapacitor electrodes, Chem. Soc. Rev. 40 (2011) 1697–1721, 40.
[30] J. Zhu, Y. Xu, J. Hua, L. Wei, J. Liu, M. Zheng, Facile synthesis of MnO_2 grown on nitrogen-doped carbon nanotubes for asymmetric supercapacitors with enhanced electrochemical performance, J. Power Sources 393 (2018) 135–144.
[31] Z. Bai, H. Li, M. Li, C. Li, X. Wang, C. Qu, et al., Flexible carbon nanotubes-MnO_2/reduced graphene oxide-polyvinylidene fluoride films for supercapacitor electrodes, Int. J. Hydrog. Energy 40 (2015) 16306–16315.
[32] J. Ji, X. Zhang, J. Liu, L. Peng, C. Chen, Z. Huang, et al., Assembly of polypyrrole nanotube@MnO_2 composites with animproved electrochemical capacitance, Mater. Sci. Eng. B 198 (2015) 51–56.
[33] P. Sun, H. Yi, T. Peng, Y. Jing, R. Wang, H. Wang, et al., Ultrathin MnO_2 nanoflakes deposited on carbon nanotube networks for symmetrical supercapacitors with enhanced performance, J. Power Sources 341 (2017) 27–35.
[34] Z. Fan, J. Chen, M. Wang, K. Cui, H. Zhou, Y. Kuang, Preparation and characterization of manganese oxide/CNT composites as supercapacitive materials, Diam. Relat. Mater. 15 (2006) 1478–1483.
[35] X. Cui, F. Hu, W. Wei, W. Chen, Dense and long carbon nanotube arrays decorated with Mn_3O_4 nanoparticles for electrodes of electrochemical supercapacitors, Carbon 49 (2011) 1225–1234.
[36] T. Zhao, S. Guo, X. Ji, Y. Zhao, X. Wang, Y. Cheng, et al., Three-dimensional heterostructured MnO2/graphene/carbon nanotube composite on Ni foam for binder-free supercapacitor electrode, Fullerenes, Nanotub. Carbon Nanostruct. 25 (2017) 391–396.
[37] C. Xiong, T. Li, A. Dang, T. Zhao, H. Li, H. Lv, Two-step approach of fabrication of three-dimensional MnO2-graphene-carbon nanotube hybrid as a binder-free supercapacitor electrode, J. Power Sources 306 (2016) 602–610.
[38] S. Wang, R.A.W. Dryfe, Graphene oxide-assisted deposition of carbon nanotubes on carbon cloth as advanced binder-free electrodes for flexible supercapacitors, J. Mater. Chem. A 1 (2013) 15279–15283.
[39] C. Zheng, H. Yang, Assembly of Ag_3PO4 nanoparticles on rose flower-like Bi_2WO_6 hierarchical architectures for achieving high photocatalytic performance, J. Mater. Sci. Mater. Electron. 29 (2018) 9291–9300.
[40] Y. Yan, H. Yang, X. Zhao, R. Li, X. Wang, Enhanced photocatalytic activity of surface disorder-engineered $CaTiO_3$, Mater. Res. Bull. 105 (2018) 286–290.
[41] J.H. Kim, Y.J. Hong, Y.C. Kang, Y.J. Choi, Y.S. Kim, Superior electrochemical properties of a-Fe_2O_3 nanofibers with a porous core/dense shell structure formed from iron acetylacetonate-polyvinylpyrrolidone composite fibers, Electrochim. Acta 154 (2015) 211–218.
[42] X. Zhu, Z. Wei, W. Zhao, X. Zhang, J. Jiang, Effects of surfactant on microstructure and electrochemical properties of $ZnMn_2O_4$ nanopowders, J. Electron. Mater. 47 (2018) 6428–6436.
[43] D.D. Purkayastha, B. Sarma, C.R. Bhattacharjee, Surfactant-assisted low-temperature synthesis of monodispersed phase purecubic CoO solid nanoparallelepipeds via thermal decomposition of cobalt(II) acetylacetonate, Mater. Lett. 107 (2013) 71–74.
[44] A. Eftekhari, Z. Fan, Ordered mesoporous carbon and its applications for electrochemical energy storage and conversion, Mater. Chem. Front. 1 (2017) 1001–1027.
[45] J. Jiang, X. He, J. Du, X. Pang, H. Yang, Z. Wei, In-situ fabrication of graphene-nickel matrix composites, Mater. Lett. 220 (2018) 178–181.
[46] Y. Lei, J. Jiang, T. Bi, J. Du, X. Pang, Tribological behavior of in situ fabricated graphene-nickel matrix composites, RSC Adv. 8 (2018) 22113.
[47] Z. Jia, T. Chen, J. Wang, J. Ni, H. Li, X. Shao, Synthesis, characterization and tribological properties of Cu/reduced graphene oxide composites, Tribol. Int. 88 (2015) 17–24.
[48] K. Wang, S. Gao, Z. Du, A. Yuan, W. Lu, L. Chen, MnO_2-Carbon nanotube composite for high-areal-density supercapacitors with high rate performance, J. Power Sources 305 (2016) 30–36.
[49] Q. Li, J. He, D. Liu, H. Yue, S. Bai, B. Liu, et al., Facile preparation of hovenia-acerba-like hierarchical MnO_2/C composites and their excellent energy storage performance for supercapacitors, J. Alloy. Comp. 693 (2017) 970–978.
[50] R. R Salunkhe, H. Ahn, J.H. Kim, Y. Yamauchi, Rational design of coaxial structured carbon nanotube-manganese oxide (CNT-MnO_2) for energy storage application, Nanotechnology 26 (2015) 204004.
[51] Y. Lei, J. Du, X. Pang, H. Wang, H. Yang, J. Jiang, Tribological properties and lubrication mechanism of in situ graphene-nickel matrix composite impregnated with lubricating oil, Mater. Res. Express 5 (2018), 056512.
[52] D. Wang, K. Wang, L. Sun, H. Wu, J. Wang, Y. Zhao, et al., MnO_2 nanoparticles anchored on carbon nanotubes with hybrid supercapacitor-battery behavior for ultrafast lithium storage, Carbon 139 (2018) 145–155.
[53] G. Zhu, Z. He, J. Chen, J. Zhao, X. Feng, Y. Ma, et al., Highly conductive three-dimensional MnO_2-carbon nanotube-graphene-Ni hybrid foam as a binder-free supercapacitor electrode, Nanoscale 6 (2014) 1079–1085.
[54] B. Chen, Y. Wang, Z. Chang, X. Wang, M. Li, X. Liu, Enhanced capacitive desalination of MnO_2 by forming composite with multi-walled carbon nanotubes, RSC Adv. 6 (2016) 6730–6736.
[55] M. Wang, Q. Yan, F. Xue, J. Zhang, J. Wang, Design and synthesis of carbon nanotubes/carbon fiber/reduced graphene oxide/MnO_2 flexible electrode material for supercapacitors, J. Phys. Chem. Solid. 119 (2018) 29–35.
[56] J. Kang, J. Wen, S.H. Jayaramb, X. Wang, S. Chen, Electrochemical characterization and equivalent circuit modeling of single-walled carbon nanotube (SWCNT) coated electrodes, J. Power Sources 234 (2013) 208–216.
[57] J. Wang, Y. Chen, B. Chen, Synthesis and control of high-performance MnO_2/carbon nanotubes nanocomposites for supercapacitors, J. Alloy. Comp. 688 (2016) 184–197.
[58] S. Kong, K. Cheng, T. Ouyang, K. Ye, G. Wang, D. Cao, Freestanding MnO_2 nanoflakes on carbon nanotube covered nickel foam as a 3D binder-free supercapacitor electrode with high performance, J. Electroanal. Chem. 786 (2017) 35–42.
[59] S. Kong, K. Cheng, T. Ouyang, Y. Gao, K. Ye, G. Wang, et al., Facile dip coating processed 3D MnO_2-graphene nanosheets/MWNT-Ni foam composites for electrochemical supercapacitors, Electrochim. Acta 226 (2017) 29–39.